nanomaterials

MDPI

Article

Ternary Polyaniline@Bi_2O_3-BiOCl nanocomposites as innovative highly active photocatalysts for the removal of the dye under solar light irradiation

Asmae Bouziani[1]*, Mohamed Yahya[2], Claudia L. Bianchi[3,4], Ermelinda Falletta[3,4] , Gokhan Celik[1],

[1]Chemical Engineering Department, Middle East Technical University, Üniversiteler, 06800, Ankara, Turkey
[2]Department of Chemistry University of Nevada, Reno 1664 North Virginia Street, Reno, Nevada 89557, USA
[3]Department of Chemistry, Università degli Studi di Milano, via C. Golgi 19, 20133 Milano, Italy
[4]Consorzio Interuniversitario Nazionale per la Scienza e Tecnologia dei Materiali (INSTM), via Giusti 9, 50121 Florence, Italy
* Correspondence: asmae@metu.edu.tr

Abstract: Ternary PANI@Bi_2O_3-BiOCl nanocomposites were successfully synthesized during the oxidative polymerization of aniline monomer in the presence of Bi_2O_3 . PANI@Bi_2O_3-BiOCl nanocomposites were characterized by several analytical techniques, including X-ray diffraction (XRD), Fourier Transform Infrared spectroscopy (FTIR), N_2 physisorption, UV-Vis Diffuse reflectance spectroscopy (DRS), X-ray photoelectron (XPS), transmission electron microscopy (TEM), and scanning electron microscopy with energy dispersive spectroscopy (SEM-EDS). The effective PANI-semiconductor interaction promotes the fast separation and transfer of photogenerated electrons and holes, enhancing the photocatalytic efficiency of the materials towards methylene blue (MB) degradation under solar light irradiation. The best results were obtained by 0.5%PANI@Bi_2O_3-BiOCl, leading to 80% MB degradation in 2h, four times higher than pristine Bi_2O_3-BiOCl. Moreover, 0.5%PANI@Bi_2O_3-BiOCl maintained stable photocatalytic performances for four cycles without significant activity loss. Various scavengers (isopropyl alcohol, formic acid, and benzoquinone) were used to identify the active species by trapping holes and radicals generated during the photocatalytic degradation process. Finally, a probable photocatalytic mechanism of PANI@Bi_2O_3-BiOCl photocatalyst was suggested.

Keywords: Nanocomposites, Polyaniline, Bi_2O_3, BiOCl, Photocatalysis, Solar light, dye

Citation: To be added by editorial staff during production.

Academic Editor: Firstname Lastname

Received: date
Revised: date
Accepted: date
Published: date

1. Introduction

Combining organic and inorganic compounds to obtain new materials displaying the properties of both components and novel performances is a well-established technique. Performing such modification by combining organic-inorganic species has extraordinary effects on the production of nano-sized materials with multifunctional applications in several fields, such as gas sensors, tissue engineering, photovoltaic cells, adsorption and photocatalysis [1-3].

Photocatalytic degradation of organic pollutants, including organic dyes, represents an important example of green technology[4-7]. This technology is based on reactive and nonselective species with a superior oxidizing capability than traditional ones (Cl_2, O_3, H_2O_2, …) [8,9] . Photocatalysis has drawn substantial attention after Fujishima and Honda described water splitting by photochemical electrodes using TiO_2 [10]. Although several conventional and commercially available semiconductors (ZnO, TiO_2, etc.)

[11-12] have been extensively investigated, their limited activity under solar light represents a significant downside for transitioning from fundamental study to practical applications. Thus, for the wide use of the solar spectrum, exploring new cost-effective and stable photocatalysts with a visible light response is of particular importance and urgency [13-19] . Bismuth-based catalysts, such as Bi_2O_3, Bi_2S_3, and BiOCl, are important semiconductor materials that have drawn significant interest due to their catalytic activity in numerous fields and being environmentally friendly[20,21] . Unfortunately, pristine Bi_2O_3 has low practical application in the field of photocatalysis because of its narrow response range of visible light and the fast recombination of electron-hole pairs, as well as the inability of the electron at the conduction band (CB) to reduce oxygen (E_{cb}= 0.33 V vs. NHE) [22]. In contrast, BiOCl is an indirect bandgap semiconductor with a high anisotropic layer structure and is chemically stable. However, its bandgap energy between 3.2 and 3.5 eV makes it a traditional UV photocatalyst. Bi_2O_3-BiOCl heterojunctions lead to better transport and separation of photogenerated charges resulting in improved photocatalytic activity due to the efficient separation of photoinduced e^-/h^+ pairs [23,24] . In recent years, conducting organic properties, particularly polyaniline (PANI), have emerged as very interesting materials for several applications, including photocatalysis. Thanks to its interesting multifunctionality and redox properties, PANI and its composites have been employed in the removal of different types of pollutants from both water and air. In fact, PANI exhibites extraordinary ability in VOCs [https://doi.org/10.1016/j.jhazmat.2017.10.012] and NO_2 [https://doi.org/10.3390/ma16031304] abatement from air matrix, as well as metals in the removal of metals and dyes from water [https://doi.org/10.1016/j.chemosphere.2021.131941; https://doi.org/10.1016/j.jece.2022.108468; https://doi.org/10.3390/polym14224897].

In fact, when used in combination with proper semiconductors, the π-π conjugated structure of the polymer can rapidly transfer the charge on the surface of the material, enhancing the separation of the photoinduced charges and reducing the recombination rate during the electron-transfer process [25-27] , improving, as a consequence, the photocatalytic activity.

Preparing PANI-semiconductor composites has drawn significant attention because of their particular electron and hole-transporting properties, simplicity of synthesis, and chemical stability [6,28-31] . Although the effect of PANI coating on traditional semiconductors, mainly TiO_2 and ZnO, has been extensively investigated, only a few studies have been dedicated to the photocatalytic properties of PANI/Bi_2O_3 composites. Recently, PANI@BiOCl has been synthesized and tested for the degradation of dyes under visible light irradiation, showing very promising results [30, 32,33] , as well as PANI@Bi_2O_3 [34,35] . However, for this latter material, more in-depth investigations are necessary to clarify the structure of the composite and, as a consequence, the role of the polymer in the photocatalytic activity of the heterostructure. In this work, a simple synthetic method leading to ternary nanocomposites (PANI@Bi_2O_3-BiOCl) characterized by enhanced photocatalytic properties is proposed. . For the first time, it has been demonstrated the formation of a second Bi(III) phase (BiOCl) during the oxidative polymerization of aniline on the surface of Bi_2O_3. The synthesized nanocomposites were tested for the photodegradation of Methyl Blue (MB), selected as a model non-biodegradable and toxic molecule, under solar light irradiation. The reusability of the more performing photocatalytic nanocomposite has been adequately investigated, indicating high stability for up to five runs. Eventually, the active species involved in the photocatalytic process were properly identified using various scavengers trapping holes and radicals.

2. Materials and Methods

2.1. Chemicals

The chemicals utilized to synthesize Bi_2O_3 nanoparticles were bismuth(III) nitrate pentahydrate ($Bi(NO_3)_3{\cdot}5H_2O$), nitric acid (HNO_3, 70%), and citric acid ($C_6H_8O_7$, 99.5%).

Also, aniline monomer (C_6H_8N), hydrochloric acid (HCl, 37%), and sodium persulfate ($Na_2S_2O_8$) were employed for polyaniline (PANI) synthesis. They were obtained from Sigma Aldrich.

Methylene Blue powder (MB, 97%), selected as organic pollutants for photocatalytic experiments, was also supplied from Sigma Aldrich.

2.1. Synthesis of Bi_2O_3

Bi_2O_3 was synthesized following the method described in the literature with some modifications [36] . More detail, 5 mmol of $Bi(NO_3)_3 \cdot 5H_2O$ was dissolved in 10 mL of 1.5 M HNO_3. Then, 10 mL of 4 M citric acid was added dropwise to the mixture under vigorous magnetic stirring for 40 min and under heating (70 °C) until it gelled. The obtained gel was dried at 80 °C overnight, then calcinated at 500 °C for 1h under air.

2.2. Preparation of PANI@Bi_2O_3-BiOCl composite

PANI@ Bi_2O_3-BiOCl composites were prepared by in situ oxidative polymerization of aniline in the presence of Bi_2O_3 nanoparticles. First, a certain amount of Bi_2O_3 nanoparticles were dispersed in 100 mL of 1 M HCl by ultrasonic vibration for 3h. Afterward, a specific amount of aniline was introduced into the mixture and stayed under stirring for 1h. Next, dropwise to the reaction mixture was added 50 mL of $Na_2S_2O_8$ (with a molar ratio aniline/oxidant of 1:2). The polymerization was maintained for 12 h under stirring at room temperature. The resultant powder was washed in abundance with distilled water and ethanol to eliminate oligoanilines and the oxidant excess. Finally, the residue (PANI@ Bi_2O_3-BiOCl) was kept for 12h in the dryer at 80 °C.

Different initial weight ratios of aniline/Bi_2O_3 (from 0.2 to 5 wt %) were tested in the experiments. For this reason, a series of PANI@Bi_2O_3-BiOCl composites having initial molar ratios of aniline/Bi_2O_3 0.2, 0.5, 1, 2, and 5 wt. % were synthesized and labeled as 0.2 PBB, 0.5 PBB, 1PBB, 2PBB, and 5 PBB, respectively.

Furthermore, the Bi_2O_3-BiOCl composite was prepared by dispersing Bi_2O_3 nanoparticles in 100 mL of 1M HCl and kept under ultrasonic vibration for 3h. Then the solution was filtrated, and the residue was washed with water and ethanol. The obtained powder was dried overnight at 80°C.

2.3. Characterization

X-ray diffraction (XRD) analyses were performed using a PANanalytical 'X'Pert PRO X-ray diffractometer with Cu Kα radiation and at 40 kV × 40 mA nominal X-ray power to characterize the phase(s) present in the resulting powders. The diffraction angles (2θ) were from 10º to 80º. The identification of the peaks from their positions and intensity was completed using the Joint Committee on Powder Diffraction Standards (JCPDS) database.

Fourier transform infrared spectroscopy (FTIR, Mattson 1000 FTIR spectrophotometer) was employed to investigate the vibration modes (ν, in cm^{-1}), dispersing the proper amount of each sample in KBr and pressing the mixture to produce disks. The scans were taken in transmission mode in a wavenumber range of 4000–500 cm^{-1} and with a resolution of 4 cm^{-1}. The samples morphology was investigated by scanning electron microscopy (SEM), performed on a Zeiss LEO 1525 field emission microscope equipped with an Inlens detector, upon metallization with chromium and an Energy Dispersive X-Ray Analyzer (EDX) BRUKER.

Transmission electron microscopy (TEM) images were compiled by a Philips 208 transmission electron microscope (FEI, Hillsboro, OR, USA). The samples were prepared by depositing a small drop of the aqueous dispersion of the solids on a copper grid precoated with a Formvar film and then evaporated in the air at room temperature.

The obtained composites' light absorption capacity and optical properties were quantified via UV-vis spectrophotometer (Varian- Cary 100) equipped with an integrat-

ing sphere and using $BaSO_4$ as a reference. The optical bandgap energy was calculated using the Kubelka-Munk function with Eq.1. [37]

$$A\,(h\nu - E_g)^{n/2} = \alpha h\nu \qquad \text{(Eq.1)}$$

where h is Planck's constant, α is absorbance, ν is light frequency, and A is the proportional constant. The parameter n differs on the semiconductor properties, n=1 and n=4 for direct and indirect bandgap, respectively. BiOCl has an indirect bandgap, so n=4, and α-Bi_2O_3 has a direct bandgap, so n=1.

M-probe apparatus (Surface Science Instruments, Pasadena, CA, USA) was adopted for X-ray photoelectron spectroscopy (XPS) analyses: the source was a monochromatic Al Kα radiation ($h\nu$= 1486.6 eV). The precision of the stated binding energies (B.E.) can be approximated as ± 0.2 eV. Peak fitting was performed via combined Gaussian−Lorentzian curves after correcting the background using the Shirley method. The binding energies were calibrated using C1s at 284.6 eV.

2.5. Photocatalytic experiments

Bi_2O_3, Bi_2O_3-BiOCl, and PBB nanopowders' photocatalytic performance was estimated by the degradation of MB under solar light illumination. Before irradiation, catalysts and the aqueous solution of MB were stirred in the dark for 20 minutes to favor the adsorption-desorption equilibrium. The length of the photocatalytic experiments was 120 min. At a specific time, a volume of the solution was taken and filtered using a filter (RC 0.45 μm). The suspension concentration was determined by measuring the prominent peak of MB in the visible range at λ= 664 nm. Photolysis tests under illumination and without a catalyst were conducted. Under the experimental conditions applied in this work, substrate photolysis was unimportant.

2.6. Identification of active species

Identifying the active species responsible for photocatalytic activity was performed via Radical species trapping tests. Formic acid (CH_2O_2, 3 mM), benzoquinone (BQ, 7.65 μM), and isopropyl alcohol (C_3H_8O, 3 mM) were used as the scavengers for holes (h^+), superoxide radicals ($^\bullet O^{2-}$), and hydroxyl radicals ($OH^\bullet$), respectively [34,38] . 1 mmol of CH_2O_2, BQ, and C_3H_8O was added into a solution of MB containing 0.5 PBB nanocomposite, and the tests were conducted as described above (2.5).

3. Results

$PANI/Bi_2O_3$ composites have been previously synthesized by other researchers [35]. Their investigations revealed only Bi(III) species as Bi_2O_3. However, our studies demonstrate that during the oxidative polymerization reaction, a second Bi(III) component is obtained in the composite, identified as BiOCl, leading to ternary nanocomposites characterized by enhanced photocatalytic properties, as described below.

3.1. Characterization

Fig. 1 shows the crystal structure of the synthesized PANI, Bi_2O_3, Bi_2O_3-BiOCl, and 0.5PBB materials investigated by XRD analysis. Pristine PANI displays an XRD pattern characterized by two low diffraction peaks at $2\theta = 20^\circ$ and 25° that can be allocated to the periodicity perpendicular and parallel to the polymer chain [39] . The XRD pattern corresponding to α-Bi_2O_3 exhibits characteristic diffraction peaks at 27o and 33o corresponding to the diffractions of the (111) and (121) plane belonging to the monoclinic phase [40] (JCPDS No.41-1449) (Fig S1). However, the XRD pattern of 0.5PBB showed diffraction peaks corresponding to two different Bi(III) species, one corresponding to α-Bi_2O_3 and another one, characterized by a higher intensity of the diffraction peaks, identified as BiOCl tetragonal phase. The crystalline peaks attributed to BiOCl are slightly

shifted to lower angles compared to pristine BiOCl. This shift can be related to the chemical interaction between PANI and Bi_2O_3-BiOCl composite, as generally observed for this type of heterostructures [41,42]. The quantitative analysis showed 87% α-Bi_2O_3 and 13% BiOCl in the 0.5PBB composite. In fact, during the oxidative polymerization step, Bi_2O_3 is dispersed in HCl solution, leading to the formation of BiOCl, according to the literature [43,44] . Fig.1 reports the diffraction pattern of Bi_2O_3 treated with HCl. It confirms that in addition to the monoclinic phases of Bi_2O_3, other diffraction peaks are present at 12.0°, 23.9° and 33.4°, corresponding to the (0 0 1), (0 0 2) and (1 0 2) plan of the BiOCl tetragonal phase (JCPDS, no. 06-0249) [40,41] . These results confirmed the formation of BiOCl when Bi_2O_3 was dispersed in HCl, resulting in the obtention of the Bi_2O_3-BiOCl heterostructure.

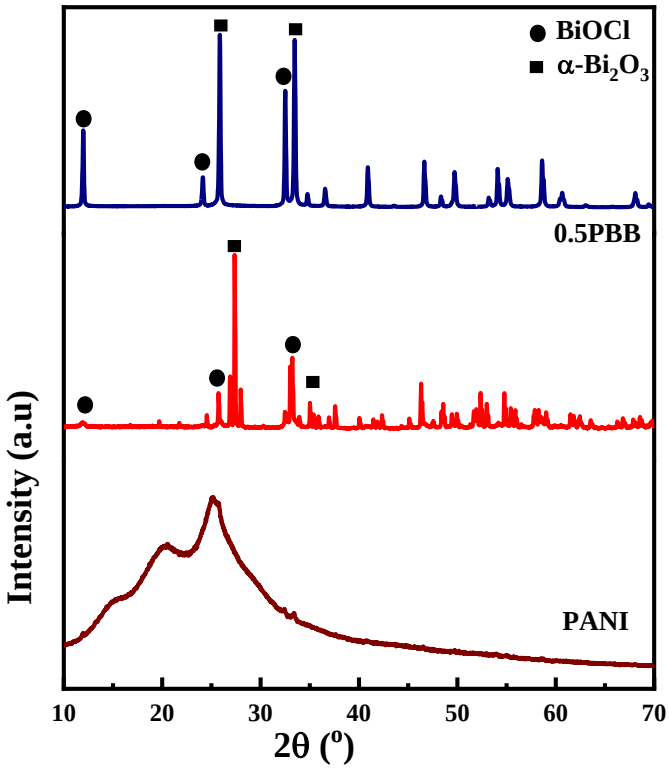

Figure 1. XRD patterns of PANI, Bi_2O_3-BiOCl, and 0.5PBB.

The efficacious insertion of Bi_2O_3-BiOCl into the PANI matrix was also determined via FTIR. Fig.2 shows the acquired spectra of Bi_2O_3-BiOCl, PANI, and 0.5PBB. Typical bands at 1571 cm^{-1} and 1465 cm^{-1} ascribed to C=N and C=C stretching vibrational modes of quinoid and benzenoid rings were recorded in the PANI's spectrum [45,46] . Likewise, the 1271 cm^{-1} band is ascribed to the C-N benzenoid stretching, while the 805 cm^{-1} is assigned to the out-of-plane deformation of C-H in the benzene ring [47] . The presence of the benzenoid and quinoid rings implies that PANI was obtained in its emeraldine form (half-oxidized) [48]. The FTIR spectrum of Bi_2O_3-BiOCl showed typical bands at 847 cm-1 and 494 cm-1, ascribed to Bi-O-Bi and Bi-O stretching, respectively. The band at 847 cm^{-1} is characteristic of Bi_2O_3 and related to the Bi-O-Bi vibration mode (Fig. S2). Moreover, the bands at 1035 and 1103 cm^{-1} can be ascribed to the symmetric and asymmetric stretching vibrations of Bi-Cl. The band at 1382 cm^{-1} is assigned to the NO^{3-} group [49]. The presence of NO^{3-} indicates a potential competition of NO^{3-} with Cl^- in

emeraldine salt structure [50]. After HCl treatment, the main band of Bi_2O_3 decreased, confirming the growth of BiOCl on Bi_2O_3 to construct the heterostructure, according to the literature [51] . The FTIR spectrum of the 0.5PBB nanocomposite exhibits the characteristic bands of both the components, organic and inorganic. The high intensity of the signals related to the polymeric components partially covers those of Bi_2O_3-BiOCl, although the typical band at 1143 cm^{-1} related to the Bi-Cl stretching vibration is well evident [52]. Eventually, the slight shift of the bands of the PANI/Bi-based materials confirms the fruitful interaction between the two components of the nanocomposite, in agreement with the XRD results.

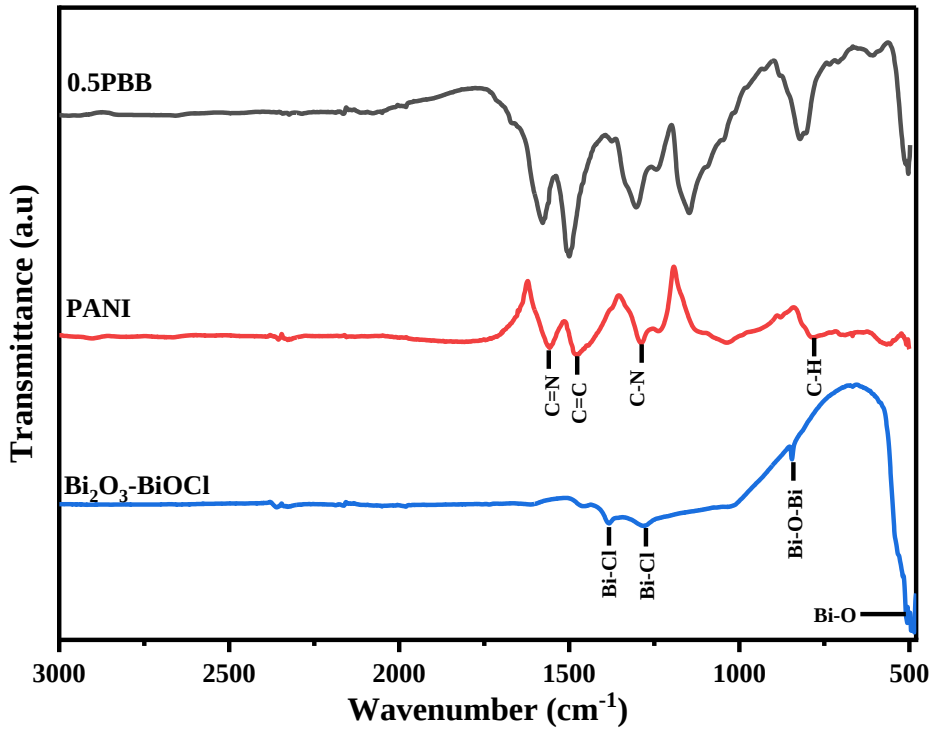

Figure 2. FTIR spectra of Bi_2O_3-BiOCl, PANI, and 0.5PBB.

SEM and TEM techniques examined the morphologies of PANI, Bi_2O_3, and 0.5PBB. The obtained images are shown in Figs.3, 4, and Fig. S3 and S4 (in the SI). The TEM and SEM images of Bi_2O_3 exhibited a spindle-like shape of about 100 nm in size, as shown in Fig.3a and S3a-c. Moreover, the EDS analysis and the O and Bi elemental mapping of Bi_2O_3 are reported in Figs S3d-f. The TEM image of PANI (Fig. 3b and 3c) showed the typical globular-like morphology, a characteristic of this polymer, as previously observed [23].

According to the results of XRD and FTIR investigations, TEM images of 0.5PBB nanocomposite showed nanocomposites containing Bi_2O_3 -BiOCl particles (dark objects) embedded into PANI matrix (Fig.3d-f) [53]. Besides, the SEM images of PANI and the 0.5PBB nanocomposite (Fig. S4a and b and d Fig.4 a and b) were acquired, as well as EDS analyses and elemental mapping were properly performed (Fig. S4c-h, Fig. S5, and Fig. 4f-m). For the composite, the SEM images were also carried out by an angle-selective backscatter detector (Fig. 4c-d), by which elements having higher atomic numbers emit backscattered electrons with greater in-

tensity. These images show that the Bi_2O_3 morphology changes upon insertion into the PANI, forming nanosheets homogenously distributed in the polymeric matrix. According to the literature, the nanosheet morphology can be attributed to the BiOCl formation [53,54]. The EDS spectrum (Fig. S5) and the elemental mapping (Fig. 4 f-m) of 0.5PBB prove the presence and homogenous distribution of Bi, O, C, and N. Furthermore, the presence of Cl can confirm the formation of the BiOCl, even if it can also be related to the use of the usual HCl dopant.

Figure 3. TEM Images of (a) Bi_2O_3, (b) and (c) PANI, (d)-(f) 0.5PBB composite.

Figure 2. TEM Images of (a) Bi_2O_3, (b) and (c) PANI, (d)-(f) 0.5PBB composite.

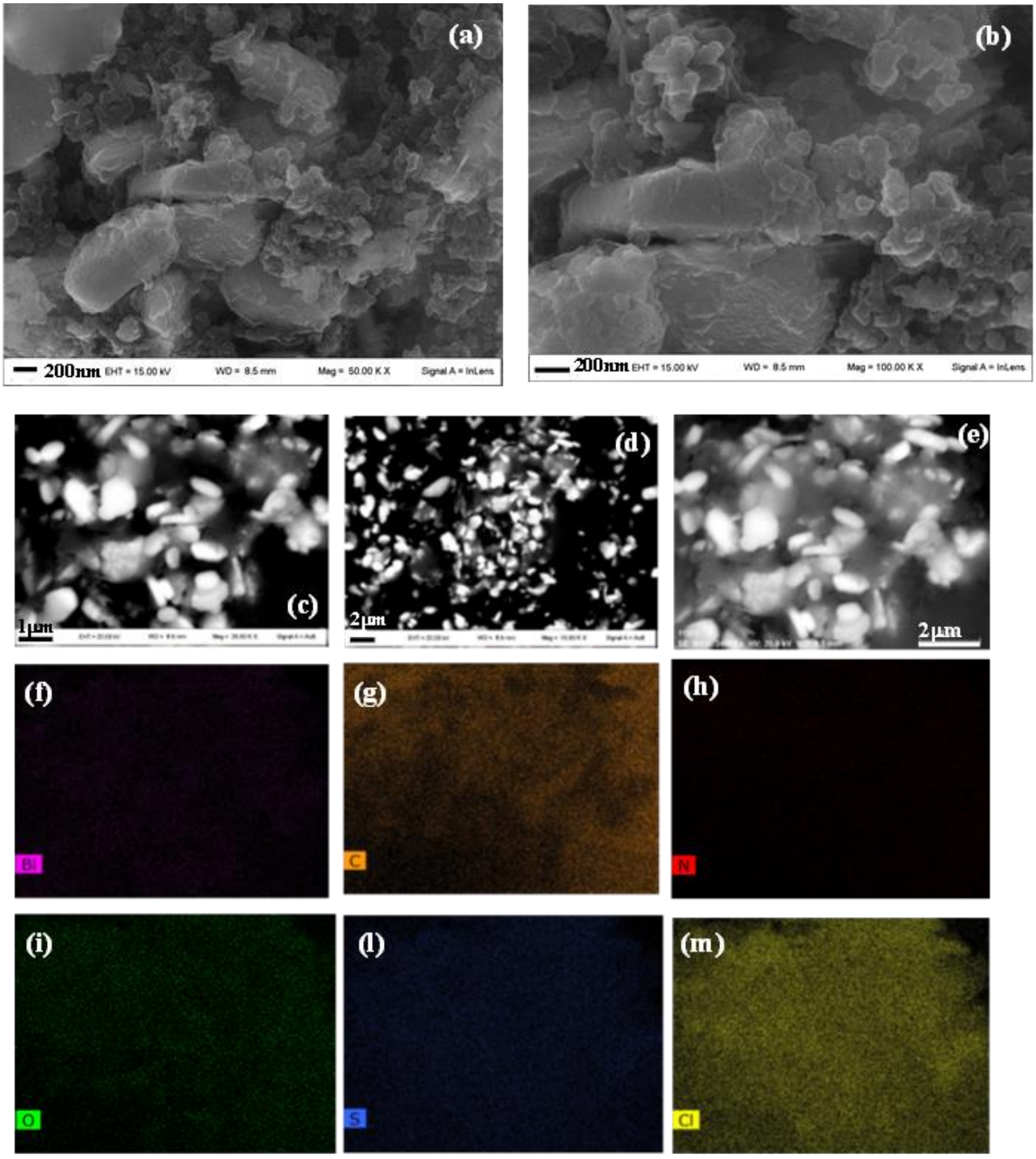

Figure 4. SEM images of 0.5PBB (a-d) and elemental mapping of (f): Bi, (g): C, (h): N, (i): O, (l): S, (m): Cl for 0.5PBB composite

XPS was used to investigate the surface element composition and chemical state of 0.5PBB and Bi_2O_3. The XPS survey of 0.5PBB (Fig. 5a) exhibits peaks related to Bi and O coming from Bi_2O_3 and BiOCl, as well as C and N from PANI. In addition, the peak of Cl can be ascribed to the presence of both BiOCl and PANI. The XPS survey of Bi_2O_3 is reported in Fig. S6. The high-resolution XPS spectra of C1s, O1s, N1s, and Bi4f are shown in Fig.5 (b-g). The deconvo-

lution of the High-Resolution spectrum of C1s (Fig. 5b) gave several parts at 284.6, 285.6, 287.3, and 291.5 eV assigned to C-C/C=C, C-N, CH, and π-π (satellite) respectively [45,55]. Fig. 5c shows the HR XPS spectrum of N1s, which can be curve-fitted into four peaks related to the presence of neutral imine nitrogen atom, neutral amine, positively charged nitrogen, and protonated imines belonging to the PANI structure [45]. The core-level spectrum fitting to O1s can be deconvoluted into two peaks (Fig. 5d) at 529.7eV and 531.3 eV assigned to Bi-O in Bi_2O_3 and a peak at 533.5eV associated with physisorbed and chemisorbed water and other surface species such as coordinated lattice oxygen, OH, and O_2 chemisorbed [37]. However, the O1s core spectrum of Bi2O3 displays only chemisorbed or physisorbed water and oxygen functionalities (Fig 5e). The HR XPS spectrum of Bi (Fig.5f and 5g) can be deconvoluted into two peaks at 159.04 eV and 164.3 eV corresponding to the signals from doublets of Bi 4f5/2 and Bi 4f7/2 in the trivalent oxidation state. Compared to the pristine Bi_2O_3 spectrum, it is evident that the peaks belonging to Bi4f of 0.5PBB shifted to higher energy, which confirms that the combination of PANI impacts the electronic energy distribution of Bi4f via the interfacial coupling interaction. The raised binding energy may be essential in effectively separating charges [56].

Figure 5. XPS results of (a) survey spectra of 0.5PBB. HR spectra of (b) C 1s, (c), N1s, (d)-(e) O1s, and (f)-(g) Bi4f of Bi_2O_3 and 0.5PBB composite.

The obtained materials' spectral characteristic and optical properties were investigated using UV-vis diffuse reflectance spectra (DRS). The spectrum corresponding to α-Bi_2O_3 (Fig. S7) displays a strong visible-light absorption, and the adsorption edge is near 411nm. In contrast, as expected, the spectrum of the Bi_2O_3-BiOCl heterostructure exhibits two absorption bands, one in the UV range (due to the presence of BiOCl) and the second one in the visible light range (Fig.6). On the other hand, the spectrum of PANI displayed 2 distinctive absorption bands, one in the near-infrared (around 350 nm) belonging to π-π* transition on the benzenoid ring and the other broad peak in the visible region between 500-700 nm assigned to the excitation transition of the benzenoid and quinoid ring (Fig.6) [57,58] . It is evident that the presence of PANI affects the light absorption characteristic of α-Bi_2O_3-BiOCl nanopowder, and the obtained composite displays a combined ability of absorption belonging to the two components. Hence, the synthesized composite gained a considerably improved absorption at the visible range compared to the pristine components, confirming the successful combination of PANI and Bi_2O_3-BiOCl.

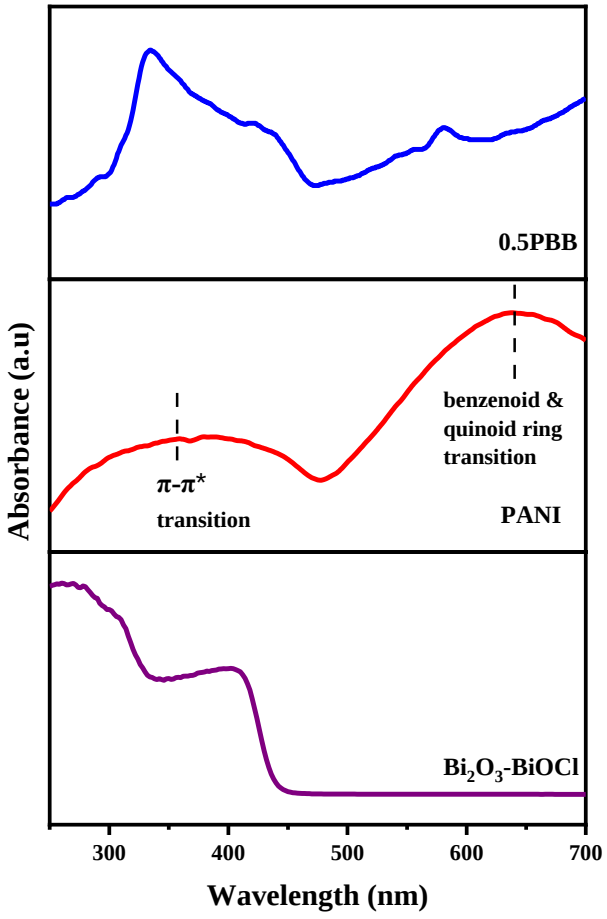

Figure 6. UV-visible spectra of Bi_2O_3-BiOCl, PANI, and 0.5PBB.

The bandgap energy of α-Bi_2O_3, Bi_2O_3-BiOCl, PANI, and 0.5PBB was calculated, and the values were 2.80 eV, 2.70 eV, 2.80 eV, and 2.52 eV, respectively. These results demonstrate that adding 0.5% of PANI resulted in narrow bandgap energy compared with pristine Bi_2O_3, PANI, and Bi_2O_3-BiOCl composite due to the hybrid's strong interaction resulting in a more apparent use of solar spectrum. Likewise, the fruitful combination of the π-conjugated structure of PANI with the Bi_2O_3-BiOCl heterostructure should result in an easy photoinduced charges migration and charge recombination restriction.

The specific surface area of Bi2O3-BiOCl, 0.2PBB,0.5PBB, 1PBB, 2PBB, and 5PBB composites were investigated via BET adsorption-desorption of nitrogen. Concerning Bi_2O_3 and Bi_2O_3-BiOCl, the specific surface area was 28.0 m^2/g and 38.2 m^2/g, respectively. The rise in the specific surface area after dispersing Bi_2O_3 in HCl could be related to the formation of BiOCl nanosheets. However, as for PBB nanocomposites, the specific surface area decreased as the PANI amount increased, and the maximum surface area was obtained for 0.2PBB composite (16.5 m^2/g). In fact, 0.5PBB, 1PBB, 2PBB, and 5PBB displayed specific surface areas of 11.6 m^2/g, 8.5 m^2/g, 6.8 m^2/g, and 6.7m^2/g, respectively. The findings are in agreement with earlier published work [59] .

The obtained isotherm belonging to 0.5PBB is given in Fig.7. 0.5PBB nanocomposite showed monolayer nitrogen adsorption at low relative pressures, where P/P_0 is less than 0.1 and a relatively small hysteresis loop at a relative pressure between 0.45-0.9. Based on the IUPAC standard classification, the N_2 adsorption/desorption isotherm is of Type IV, indicating that the structure of 0.5PBB is mesoporous.

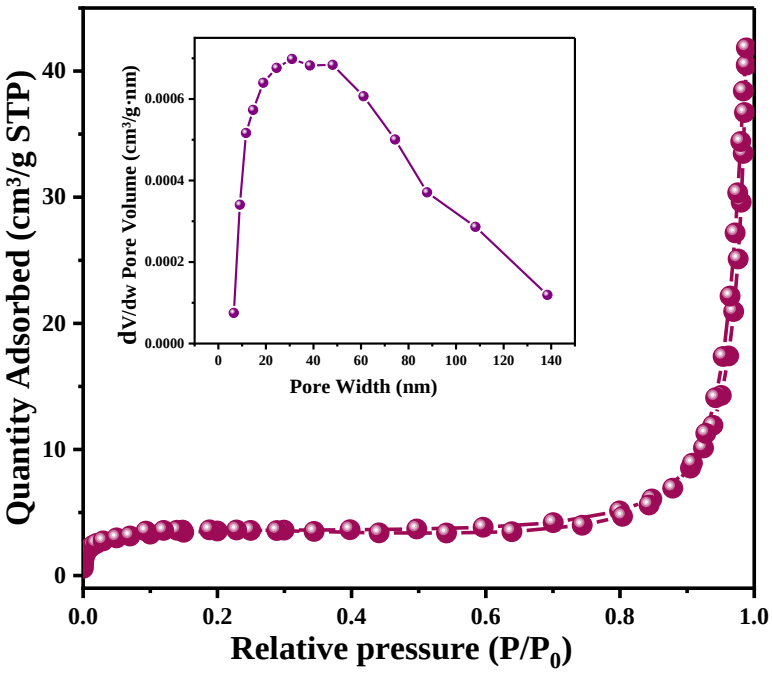

Figure 7. N_2 adsorption-desorption isotherm of 0.5PBB composite.

3.2. Photocatalytic test

The photocatalytic performance of the materials was studied by following the photodegradation of MB under solar light irradiation at ambient temperature. The photodegradation efficacy in the absence of any material (photolysis) and the presence of α-Bi_2O_3 nanopowder and PBB nanocomposites are displayed in Fig.S8. In the absence of the photocatalyst, the photodegradation is negligible, as well as when the reaction is carried out in the dark. As expected, PANI shows no activity towards MB removal under visible light. In fact, the abatement of MB reached only 20% after 120 min (Fig.S8). The Bi_2O_3 nanopowder displayed 38% degradation after 120 min irradiation (Fig.S8). These results agree with the previous reports [60] . Combining Bi_2O_3-BiOCl with PANI results in an apparent enhancement in photocatalytic activity. The found photodegradation efficiency for 0.2PBB, 0.5PBB, 1PBB, 2PBB, and 5PBB was 60%, 80%, 55%, 50%, and 29%, respectively (Fig.8). From these outcomes, it can be assumed that the PANI amount added is a crucial factor affecting photocatalytic degradation efficacy. Inserting PANI into Bi_2O_3-BiOCl enhances the photocatalytic efficiency; however, too much PANI has the opposite impact. As reported above, the maximum photodegradation activity was obtained for 0.5PBB nanocomposite (Fig.8), reaching an MB degradation of 80% after 2h. It is evident that a good dispersion of PANI in Bi_2O_3-BiOCl is related to the amount of PANI added, which leads to the transfer and separation of charge carriers while conserving the surface availability for oxidation. In contrast, if the amount of PANI exceeds a certain amount, it may limit contact with the oxidation site due to the surface coverage [49]. Plotting $\ln(C/C_0)$ versus illumination time (Fig.S9) linear curves were obtained, suggesting that the MB photodegradation by PBB is a pseudo-first-order reaction. Fig.9a displays the apparent constant rate (k) for the composites having various PANI amounts. The maximum K value was 0.012 min^{-1} for 0.5 PBB, which is four times higher than that of pristine Bi_2O_3-BiOCl (0.003 min^{-1}), confirming the fruitful interaction between PANI and Bi_2O_3-BiOCl leading to enhanced photocatalytic activity. The catalytic activity of the ternary PANI@Bi_2O_3-BiOCl reported in this study was bettter than the one reported when PANI@Bi2O3 and PANI@BiOCl used [33,34].

The photocatalyst re-usage for several runs is a vital factor for applications. For this purpose, the 0.5PBB nanocomposite was analyzed for 4 cycle runs. At the end of each cycle, the catalyst was retrieved via centrifugation and immediately reused without any treatment. Fig.9b displays the obtained results. It is worth stating that the 0.5PBBB catalyst showed good stability up to four cycles, however exhibiting a gradual slow decrease in photoactivity. Starting from an initial 80% of photodegradation at the photoactivity dropped to 70% during the fourth cycle, which could be due to nanoparticles' aggregation and/or irreversible adsorption of the dye transformation product on the surface of the polymeric matrix leading to the blockage of photocatalytic active sites.

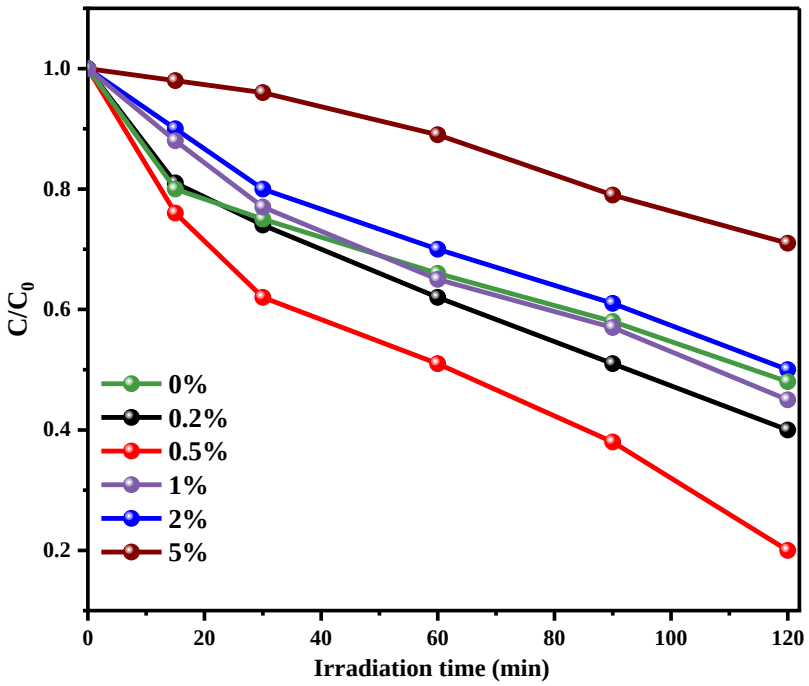

Figure 8. Conversion plots for the MB photodegradation for synthesized composite under solar light irradiation

Figure 9. (a) Rate constant of Bi_2O_3-BiOCl and PBB composites. (b) Reuse of 0.5PBB for the photocatalytic degradation of MB under solar light illumination.

3.3. Identification of active species

Numerous radical trapping tests for MB degradation in the presence of 0.5 PBB under solar light irradiation were carried out to understand the photocatalytic mechanism occurring on the PBB composites. C_3H_8O, CH_2O_2, and BQ were used to trap $OH^{\bullet}$, h+, and $^{\bullet}O^{2-}$, respectively. Fig.10 shows that the addition of C_3H_8O caused a reduction in the photocatalytic

efficiency from 80% to 30%. These findings demonstrate the key role of $OH^{\bullet}$ in the photocatalytic process. Similarly, a considerable decrease in the photocatalytic activity was observed from 80% to 57% after adding CH_2O_2, meaning h^+ is another major oxidizing species. On the contrary, upon adding BQ, the efficiency showed a negligible drop, implying that $^{\bullet}O^{2-}$ is not an active radical specie in the MB photodegradation. It can be assumed from these outcomes that the active species influencing most of the photo-oxidative degradation of MB by 0.5 PBB are $OH^{\bullet}$ and h^+. Other researchers reported similar results [32,41].

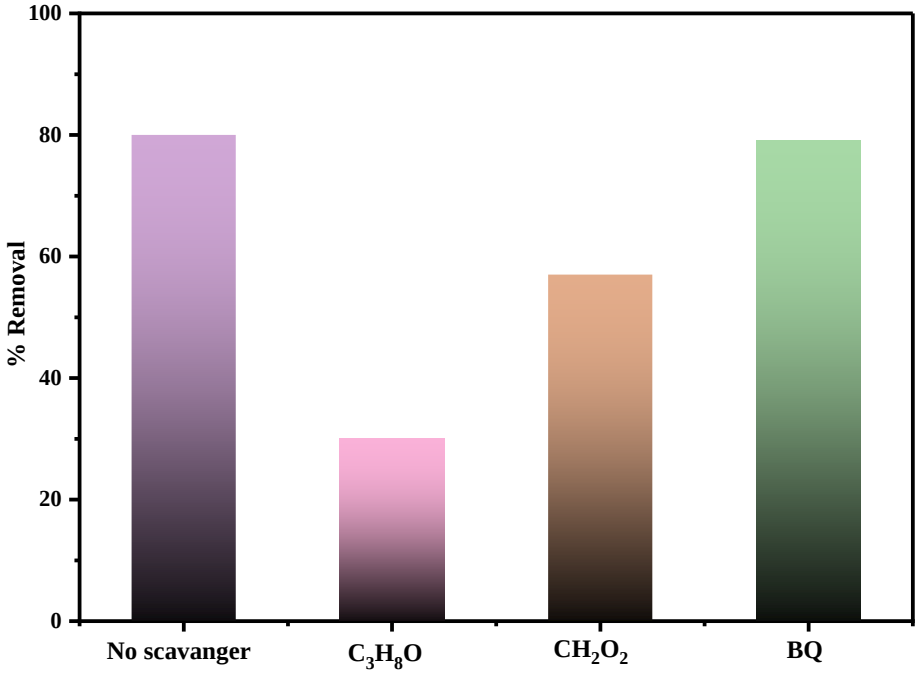

Figure 10. MB Photocatalytic degradation by 0.5PBB composite upon solar light irradiation in the presence of scavengers (C_3H_8, CH_2O_2, and BQ).

3.4. Photocatalytic mechanism

The photocatalytic results show that the coating of Bi_2O_3-BiOCl with PANI led to increased photocatalytic efficiency. However, increasing the amount of PANI above 0.5% (wt.) caused a reduction in the photocatalytic degradation of MB, presumably due to excess PANI blocking contact with the oxidation site because of the surface coverage [61] . The photo-oxidation of the species absorbed at the surface of Bi_2O_3-BiOCl is limited by the position of the conduction band minimum (CBM) and valence band maximum (VBM). To examine the effect of PANI addition on the PBB bandgap structure, the CBM and VBM were determined theoretically, and the obtained values are presented in Fig. 11. The conduction band (Ec) energy was calculated using Eq.2 [62,63] .

$$E_c = X - E + 0.5E_g \qquad \text{Eq. 2}$$

E_c: semiconductor edge conduction band at 0 charge point, X: absolute electronegativity of semiconductor (Mulliken) (X=5.95 eV and 5.0 eV for Bi_2O_3 and BiOCl, respectively), computed from the electronegativity absolute geometric mean of the constituent atoms, defined as the atomic electronic affinity arithmetic means and the energy of the first ionization. E is the energy of free electrons on the hydrogen scale (~4.5 eV), and E_g is the bandgap energy of the semiconductor.

The Eg of α-Bi_2O_3, BiOCl, and PANI are 2.8, 3.21[19], and 2.8 eV, respectively. The conduction band potentials for α-Bi_2O_3 and BiOCl are +0.21 and -1.11 eV, and the valence band potentials are +3.01 and +2.10 eV, respectively. Whereas HOMO and LUMO of PANI are 0.8 eV and -1.9 eV (vs. NHE) [64] .

The visible illumination efficiently generates electron transition from VB to the CB for samples with low bandgap values, causing an equal amount of unoccupied sites. Besides, a fraction of electron-hole (e^-/h^+) pairs recombine, and the input energy is emitted as heat or light. This recombination is balanced by an electron transition from VB to CB. In order to improve the photocatalytic activity, the optimization of electron transition and the e^-/h^+ pairs must be performed. Thus, the photocatalyst with the appropriate Eg displayed an enhanced degradation rate.

Theoretically and based on the heterostructure transfer of photogenerated carriers, PANI can inject electrons into the CB of Bi_2O_3. Then, the holes present at the VB of Bi_2O_3 can be transferred to the VB of BiOCl via the heterostructure formed, leading to an efficient e^-/h^+ separation [30,60] . However, the CB of Bi_2O_3 is less negative (+0.21 eV) than the $O_2/O_2^{\bullet-}$ potential (-0.33 eV vs. NHE), signifying the photogenerated electrons at the Bi_2O_3 CB are incapable of reducing O_2 and generating $O_2^{\bullet-}$ [32]. These findings confirm the results of the active species trapping investigation, which stated that $O_2^{\bullet-}$ does not take part in the photodegradation of MB.

Based on the findings obtained from radical scavengers experiments, a mechanism for the photocatalytic performance was given in Fig.11. Under sun-illumination, PANI and Bi_2O_3 are excited due to their low bandgap energy, and the photoelectrons and holes are formed. Since the LUMO potential of PANI and the CB of Bi_2O_3 are more negative than the CB of BiOCl, the photoinduced electrons of PANI and Bi2O3 will migrate into the CB of BiOCl [61,65] . Thus, the delay of the e^-/h^+ recombination is due to the efficiency of photogenerated electrons and holes separation, which is crucial for enhancing photocatalytic activity. The charge separation efficiently lowers the recombination rate of electron/hole, thus improving the photocatalytic performance at the ternary α-Bi_2O_3@BiOCl@ PANI composite. According to the experimental outcomes, the plausible photocatalytic mechanisms are given in Eq.(3)–(6):

$$PANI@Bi_2O_3 - BiOCl + hv \rightarrow h^+ + e^+ \quad (3)$$

$$H_2O^- + h^+ \rightarrow OH^\bullet \quad (4)$$

$$h^+ + MB \rightarrow Degradation\ products \quad (5)$$

$$OH^\bullet + MB \rightarrow Degradation\ products \quad (6)$$

Figure 11. Schematic photocatalytic mechanism of photocatalyst PB composite.

4. Conclusion

In summary, ternary polyaniline@Bi_2O_3-BiOCl nanocomposite photocatalysts with various amounts of PANI were efficiently obtained via in situ polymerization of aniline in the presence of Bi_2O_3. XRD, FTIR, TEM, SEM-EDS, XPS, and DRS techniques were used to confirm the synthesis of composites. The third Bi(III) phase (BiOCl) was obtained during the in situ the polymerization step. The results show that the addition of PANI up to 1% increased the photocatalytic activity of the nanocomposite. Furthermore, 0.5PBB composite demonstrated the maximum photocatalytic degradation efficacy, degrading 80% of MB after two hours of solar light illumination. The enhancement in photocatalytic activity is associated with forming a heterostructure between α-Bi_2O_3, BiOCl, and PANI, promoting the photogenerated e^-/h^+ pairs separation. However, adding too much PANI had a negative effect due to limit contact with the oxidation site due to the surface coverage. The nanocomposite was stable for all the investigated cycles, always maintaining high MB photodegradation values. The scavenger test established that hole h^+ and $OH^\bullet$ radicals are the active radical species in the photocatalytic process. The efficient charge separation enhanced interfacial charge transfer and the higher activity of the adsorption sites are primarily due to the positive synergetic effect between PANI and Bi_2O_3-BiOCl.

References

1. Liao, G.; Li, Q.; Xu, Z. The Chemical Modification of Polyaniline with Enhanced Properties: A Review. Prog Org Coat 2019, 126, 35–43, doi:10.1016/J.PORGCOAT.2018.10.018.

2. Zhu, S.; Khan, M.A.; Kameda, T.; Xu, H.; Wang, F.; Xia, M.; Yoshioka, T. New Insights into the Capture Performance and Mechanism of Hazardous Metals Cr3+ and Cd2+ onto an Effective Layered Double Hydroxide Based Material. J Hazard Mater 2022, 426, 128062, doi:10.1016/J.JHAZMAT.2021.128062.

3. Zhu, S.; Chen, Y.; Khan, M.A.; Xu, H.; Wang, F.; Xia, M. In-Depth Study of Heavy Metal Removal by an Etidronic Acid-Functionalized Layered Double Hydroxide. ACS Appl

Mater Interfaces 2022, 14, 7450–7463, doi:10.1021/ACSAMI.1C22035/ASSET/IMAGES/LARGE/AM1C22035_0011.JPEG.

4. Mimouni, I.; Bouziani, A.; Naciri, Y.; Boujnah, M.; El Belghiti, M.A.; El Azzouzi, M. Effect of Heat Treatment on the Photocatalytic Activity of α-Fe2O3 Nanoparticles: Towards Diclofenac Elimination. Environmental Science and Pollution Research 2021, 1–13, doi:10.1007/S11356-021-16146-W/FIGURES/13.

5. Naciri, Y.; Ait Ahsaine, H.; Chennah, A.; Amedlous, A.; Taoufyq, A.; Bakiz, B.; Ezahri, M.; Villain, S.; Benlhachemi, A. Facile Synthesis, Characterization and Photocatalytic Performance of Zn3(PO4)2 Platelets toward Photodegradation of Rhodamine B Dye. J Environ Chem Eng 2018, 6, 1840–1847, doi:10.1016/J.JECE.2018.02.009.

6. Liu, L.; Ding, L.; Liu, Y.; An, W.; Lin, S.; Liang, Y.; Cui, W. A Stable Ag3PO4@PANI Core@shell Hybrid: Enrichment Photocatalytic Degradation with π-π Conjugation. Appl Catal B 2017, 201, 92–104, doi:10.1016/j.apcatb.2016.08.005.

7. Naciri, Y.; Hsini, A.; Ajmal, Z.; Navío, J.A.; Bakiz, B.; Albourine, A.; Ezahri, M.; Benlhachemi, A. Recent Progress on the Enhancement of Photocatalytic Properties of BiPO4 Using π–Conjugated Materials. Adv Colloid Interface Sci 2020, 280, 102160, doi:10.1016/J.CIS.2020.102160.

8. Naciri, Y.; Chennah, A.; Jaramillo-Páez, C.; Navío, J.A.; Bakiz, B.; Taoufyq, A.; Ezahri, M.; Villain, S.; Guinneton, F.; Benlhachemi, A. Preparation, Characterization and Photocatalytic Degradation of Rhodamine B Dye over a Novel Zn3(PO4)2/BiPO4 Catalyst. J Environ Chem Eng 2019, 7, 103075, doi:10.1016/J.JECE.2019.103075.

9. Liu, X.; Jin, A.; Jia, Y.; Xia, T.; Deng, C.; Zhu, M.; Chen, C.; Chen, X. Synergy of Adsorption and Visible-Light Photocatalytic Degradation of Methylene Blue by a Bifunctional Z-Scheme Heterojunction of WO3/g-C3N4. Appl Surf Sci 2017, 405, 359–371, doi:10.1016/J.APSUSC.2017.02.025.

10. Fujishima, A.; Honda, K. Electrochemical Photolysis of Water at a Semiconductor Electrode. Nature 1972, 238, 37–38, doi:10.1038/238037a0.

11. Meroni, D.; Bianchi, C.L.; Boffito, D.C.; Cerrato, G.; Bruni, A.; Sartirana, M.; Falletta, E. Piezo-Enhanced Photocatalytic Diclofenac Mineralization over ZnO. Ultrason Sonochem 2021, 75, doi:10.1016/J.ULTSONCH.2021.105615.

12. Meroni, D.; Jiménez-Salcedo, M.; Falletta, E.; Bresolin, B.M.; Kait, C.F.; Boffito, D.C.; Bianchi, C.L.; Pirola, C. Sonophotocatalytic Degradation of Sodium Diclofenac Using Low Power Ultrasound and Micro Sized TiO2. Ultrason Sonochem 2020, 67, 105123, doi:10.1016/J.ULTSONCH.2020.105123.

13. Bouziani, A.; Park, J.; Ozturk, A. Synthesis of α-Fe2O3/TiO2 Heterogeneous Composites by the Sol-Gel Process and Their Photocatalytic Activity. J Photochem Photobiol A Chem 2020, 400, 112718, doi:10.1016/j.jphotochem.2020.112718.

14. Naciri, Y.; Ait Ahsaine, H.; Chennah, A.; Amedlous, A.; Taoufyq, A.; Bakiz, B.; Ezahri, M.; Villain, S.; Benlhachemi, A. Facile Synthesis, Characterization and Photocatalytic Performance of Zn3(PO4)2 Platelets toward Photodegradation of Rhodamine B Dye. J Environ Chem Eng 2018, 6, 1840–1847, doi:10.1016/J.JECE.2018.02.009.

15. Naciri, Y.; Hsini, A.; Ajmal, Z.; Bouddouch, A.; Bakiz, B.; Navío, J.A.; Albourine, A.; Valmalette, J.C.; Ezahri, M.; Benlhachemi, A. Influence of Sr-Doping on Structural, Optical and Photocatalytic Properties of Synthesized Ca3(PO4)2. J Colloid Interface Sci 2020, 572, 269–280, doi:10.1016/J.JCIS.2020.03.105.

16. Bouziani, A.; Park, J.; Ozturk, A. Effects of Fluorination and Thermal Shock on the Photocatalytic Activity of Bi2O3 Nanopowders. Colloids Surf A Physicochem Eng Asp 2021, 626, 127049, doi:10.1016/J.COLSURFA.2021.127049.

17. Gündoğmuş, P.; Park, J.; Öztürk, A. Preparation and Photocatalytic Activity of G-C3N4/TiO2 Heterojunctions under Solar Light Illumination. Ceram Int 2020, 46, 21431–21438, doi:10.1016/J.CERAMINT.2020.05.241.

18. Das, T.K.; Ganguly, S.; Bhawal, P.; Remanan, S.; Mondal, S.; Das, N.C. Mussel Inspired Green Synthesis of Silver Nanoparticles-Decorated Halloysite Nanotube Using Dopamine: Characterization and Evaluation of Its Catalytic Activity. Applied Nanoscience (Switzerland) 2018, 8, 173–186, doi:10.1007/S13204-018-0658-3/FIGURES/15.

19. Das, T.K.; Remanan, S.; Ghosh, S.; Ghosh, S.K.; Das, N.C. Efficient Synthesis of Catalytic Active Silver Nanoparticles Illuminated Cerium Oxide Nanotube: A Mussel Inspired Approach. Environ Nanotechnol Monit Manag 2021, 15, 100411, doi:10.1016/J.ENMM.2020.100411.

20. Raza, W.; Bahnemann, D.; Muneer, M. A Green Approach for Degradation of Organic Pollutants Using Rare Earth Metal Doped Bismuth Oxide. Catal Today 2018, 300, 89–98, doi:10.1016/J.CATTOD.2017.07.029.

21. Raza, W.; Khan, A.; Alam, U.; Muneer, M.; Bahnemann, D. Facile Fabrication of Visible Light Induced Bi2O3 Nanorod Using Conventional Heat Treatment Method. J Mol Struct 2016, 1107, 39–46, doi:10.1016/J.MOLSTRUC.2015.11.014.

22. Jiang, H.Y.; Cheng, K.; Lin, J. Crystalline Metallic Au Nanoparticle-Loaded α-Bi2O3 Microrods for Improved Photocatalysis. Physical Chemistry Chemical Physics 2012, 14, 12114–12121, doi:10.1039/C2CP42165H.

23. Kong, S.; An, Z.; Zhang, W.; An, Z.; Yuan, M.; Chen, D. Preparation of Hollow Flower-Like Microspherical β-Bi2O3/BiOCl Heterojunction and High Photocatalytic Property for Tetracycline Hydrochloride Degradation. Nanomaterials 2020, 10, doi:10.3390/NANO10010057.

24. Liu, H.Z.; Han, Q.F.; Ding, H.W.; Yu, H.M.; Chiu, T.W. One-Step Route to α-Bi2O3/BiOX (X = Cl, Br) Heterojunctions with Bi2O3 Ultrafine Nanotubes Closely Adhered to BiOX Nanosheets. J Taiwan Inst Chem Eng 2022, 131, 104147, doi:10.1016/J.JTICE.2021.11.014.

25. Zhang, J.; Shu, D.; Zhang, T.; Chen, H.; Zhao, H.; Wang, Y.; Sun, Z.; Tang, S.; Fang, X.; Cao, X. Capacitive Properties of PANI/MnO2 Synthesized via Simultaneous-Oxidation Route. J Alloys Compd 2012, 532, 1–9, doi:10.1016/j.jallcom.2012.04.006.

26. Pandimurugan, R.; Thambidurai, S. Synthesis of Seaweed-ZnO-PANI Hybrid Composite for Adsorption of Methylene Blue Dye. J Environ Chem Eng 2016, 4, 1332–1347, doi:10.1016/j.jece.2016.01.030.

27. Guo, N.; Liang, Y.; Lan, S.; Liu, L.; Zhang, J.; Ji, G.; Gan, S. Microscale Hierarchical Three-Dimensional Flowerlike TiO2/PANI Composite: Synthesis, Characterization, and Its Remarkable Photocatalytic Activity on Organic Dyes under UV-Light and Sunlight Irradiation. Journal of Physical Chemistry C 2014, 118, 18343–18355, doi:10.1021/jp5044927.

28. Ge, L.; Han, C.; Liu, J. In Situ Synthesis and Enhanced Visible Light Photocatalytic Activities of Novel PANI-g-C3N4 Composite Photocatalysts. J Mater Chem 2012, 22, 11843–11850, doi:10.1039/c2jm16241e.

29. Sharma, D.; Singh, T. A DFT Study of Polyaniline/ZnO Nanocomposite as a Photocatalyst for the Reduction of Methylene Blue Dye. J Mol Liq 2019, 293, 111528, doi:10.1016/j.molliq.2019.111528.

30. Wang, Q.; Hui, J.; Li, J.; Cai, Y.; Yin, S.; Wang, F.; Su, B. Photodegradation of Methyl Orange with PANI-Modified BiOCl Photocatalyst under Visible Light Irradiation. Appl Surf Sci 2013, 283, 577–583, doi:10.1016/j.apsusc.2013.06.149.

31. Falletta, E.; Bruni, A.; Sartirana, M.; Boffito, D.C.; Cerrato, G.; Giordana, A.; Djellabi, R.; Khatibi, E.S.; Bianchi, C.L. Solar Light Photoactive Floating Polyaniline/TiO2 Composites for Water Remediation. Nanomaterials 2021, Vol. 11, Page 3071 2021, 11, 3071, doi:10.3390/NANO11113071.

32. Mansor, E.S.; Geioushy, R.A.; Fouad, O.A. PANI/BiOCl Nanocomposite Induced Efficient Visible-Light Photocatalytic Activity. Journal of Materials Science: Materials in Electronics 2021, 32, 1992–2000, doi:10.1007/S10854-020-04966-4/FIGURES/12.

33. Wang, J.; Hao, X.; Jiang, Y.; Zhang, D.; Ren, L.; Gong, J.; Wu, X.; Zhang, Y.; Tong, Z. Synthesis, Structure, and Photocatalytic Activity of PANI/BiOCl Nanocomposites. Mater Res Express 2019, 6, 0850c1, doi:10.1088/2053-1591/AB1FA5.

34. Dai, J.; Chen, X.; Yang, H. Visible Light Photocatalytic Degradation of Dyes by a New Polyaniline/β-Bi2O3 Composite. http://dx.doi.org/10.1080/24701556.2017.1284128 2017, 47, 1364–1368, doi:10.1080/24701556.2017.1284128.

35. Li, B.; Li, Y.; Kang, Y. Simple Hydrothermal Preparation of Novel Bi2O3/PANI Heterojunction with Significantly Enhanced Visible-Light Photocatalytic Activity and Stability. Mater Lett 2021, 286, 129226, doi:10.1016/J.MATLET.2020.129226.

36. Hameed, A.; Montini, T.; Gombac, V.; Fornasiero, P. Surface Phases and Photocatalytic Activity Correlation of Bi 2 O 3 /Bi 2 O 4-x Nanocomposite. J Am Chem Soc 2008, 130, 9658–9659, doi:10.1021/JA803603Y/SUPPL_FILE/JA803603Y-FILE002.PDF.

37. Jaramillo-Páez, C.; Navío, J.A.; Hidalgo, M.C.; Bouziani, A.; Azzouzi, M. El Mixed α-Fe2O3/Bi2WO6 Oxides for Photoassisted Hetero-Fenton Degradation of Methyl Orange and Phenol. J Photochem Photobiol A Chem 2017, 332, 521–533, doi:10.1016/j.jphotochem.2016.09.031.

38. Wang, Y.; He, J.; Wu, P.; Luo, D.; Yan, R.; Zhang, H.; Jiang, W. Simultaneous Removal of Tetracycline and Cu(II) in Hybrid Wastewater through Formic-Acid-Assisted TiO2Photocatalysis. Ind Eng Chem Res 2020, 59, 15098–15108, doi:10.1021/ACS.IECR.0C02443/ASSET/IMAGES/LARGE/IE0C02443_0012.JPEG.

39. Guo, N.; Liang, Y.; Lan, S.; Liu, L.; Zhang, J.; Ji, G.; Gan, S. Microscale Hierarchical Three-Dimensional Flowerlike TiO2/PANI Composite: Synthesis, Characterization, and Its

Remarkable Photocatalytic Activity on Organic Dyes under UV-Light and Sunlight Irradiation. Journal of Physical Chemistry C 2014, 118, 18343–18355, doi:10.1021/JP5044927.

40. Chai, S.Y.; Kim, Y.J.; Jung, M.H.; Chakraborty, A.K.; Jung, D.; Lee, W.I. Heterojunctioned BiOCl/Bi2O3, a New Visible Light Photocatalyst. J Catal 2009, 262, 144–149, doi:10.1016/J.JCAT.2008.12.020.

41. Khairy, M.; Bayoumy, W.A.; Qasim, K.F.; El-Shereafy, E.; Mousa, M.A. Ternary V-Doped Li4Ti5O12-Polyaniline-Graphene Nanostructure with Enhanced Electrochemical Capacitance Performance. Materials Science and Engineering: B 2021, 271, 115312, doi:10.1016/J.MSEB.2021.115312.

42. Mannaa, M.A.; Qasim, K.F.; Alshorifi, F.T.; El-Bahy, S.M.; Salama, R.S. Role of NiO Nanoparticles in Enhancing Structure Properties of TiO2and Its Applications in Photodegradation and Hydrogen Evolution. ACS Omega 2021, 6, 30386–30400, doi:10.1021/ACSOMEGA.1C03693/ASSET/IMAGES/LARGE/AO1C03693_0015.JPEG.

43. Tang, X.; Ma, C.; Liu, N.; Liu, C.; Liu, S. Visible Light β-Bi2O3/BiOCl Heterojunction Photocatalyst with Highly Enhanced Photocatalytic Activity. Chem Phys Lett 2018, 709, 82–87, doi:10.1016/J.CPLETT.2018.08.045.

44. Zhao, Q.; Liu, X.; Xing, Y.; Liu, Z.; Du, C. Synthesizing Bi2O3/BiOCl Heterojunctions by Partial Conversion of BiOCl. J Mater Sci 2017, 52, 2117–2130, doi:10.1007/S10853-016-0499-Y/FIGURES/11.

45. Hsini, A.; Naciri, Y.; Laabd, M.; Bouziani, A.; Navío, J.A.; Puga, F.; Boukherroub, R.; Lakhmiri, R.; Albourine, A. Development of a Novel PANI@WO3 Hybrid Composite and Its Application as a Promising Adsorbent for Cr(VI) Ions Removal. J Environ Chem Eng 2021, 9, 105885, doi:10.1016/J.JECE.2021.105885.

46. Hsini, A.; Benafqir, M.; Naciri, Y.; Laabd, M.; Bouziani, A.; Ez-zahery, M.; Lakhmiri, R.; Alem, N. El; Albourine, A. Synthesis of an Arginine-Functionalized Polyaniline@FeOOH Composite with High Removal Performance of Hexavalent Chromium Ions from Water: Adsorption Behavior, Regeneration and Process Capability Studies. Colloids Surf A Physicochem Eng Asp 2021, 617, 126274, doi:10.1016/J.COLSURFA.2021.126274.

47. Jagadeesh Babu, V.; Vempati, S.; Ramakrishna, S. Conducting Polyaniline-Electrical Charge Transportation. Materials Sciences and Applications 2013, 2013, 1–10, doi:10.4236/MSA.2013.41001.

48. Laabd, M.; Imgharn, A.; Hsini, A.; Naciri, Y.; Mobarak, M.; Szunerits, S.; Boukherroub, R.; Albourine, A. Efficient Detoxification of Cr(VI)-Containing Effluents by Sequential Adsorption and Reduction Using a Novel Cysteine-Doped PANi@faujasite Composite: Experimental Study Supported by Advanced Statistical Physics Prediction. J Hazard Mater 2022, 422, 126857, doi:10.1016/J.JHAZMAT.2021.126857.

49. Li, W. Facile Synthesis of Monodisperse Bi2O3 Nanoparticles. Mater Chem Phys 2006, 99, 174–180, doi:10.1016/J.MATCHEMPHYS.2005.11.007.

50. Astuti, Y.; Fauziyah, A.; Nurhayati, S.; Wulansari, A.D.; Andianingrum, R.; Hakim, A.R.; Bhaduri, G. Synthesis of α-Bismuth Oxide Using Solution Combustion Method and Its Photocatalytic Properties. IOP Conf Ser Mater Sci Eng 2016, 107, 012006, doi:10.1088/1757-899X/107/1/012006.

51. Ruiz-Castillo, A.L.; Hinojosa-Reyes, M.; Camposeco-Solis, R.; Ruiz, F. Photocatalytic Activity of Bi2O3/BiOCl Heterojunctions Under UV and Visible Light Illumination for Degradation of Caffeine. Top Catal 2022, 65, 1071–1087, doi:10.1007/S11244-022-01644-Z/FIGURES/13.

52. Tang, W.; Zhang, Y.; Guo, H.; Liu, Y. Heterogeneous Activation of Peroxymonosulfate for Bisphenol AF Degradation with BiOI0.5Cl0.5. RSC Adv 2019, 9, 14060–14071, doi:10.1039/C9RA01687B.

53. Yang, X.; Sun, S.; Cui, J.; Yang, M.; Luo, Y.; Liang, S. Synthesis, Functional Modifications, and Diversified Applications of Hybrid BiOCl-Based Heterogeneous Photocatalysts: A Review. Cryst Growth Des 2021, 21, 6576–6618, doi:10.1021/ACS.CGD.1C00866/ASSET/IMAGES/LARGE/CG1C00866_0006.JPEG.

54. Geng, J.; Hou, W.H.; Lv, Y.N.; Zhu, J.J.; Chen, H.Y. One-Dimensional BiPO4 Nanorods and Two-Dimensional BiOCl Lamellae: Fast Low-Temperature Sonochemical Synthesis,Characterization, and Growth Mechanism. Inorg Chem 2005, 44, 8503–8509, doi:10.1021/IC050674G.

55. Chen, S.; Huang, D.; Zeng, G.; Gong, X.; Xue, W.; Li, J.; Yang, Y.; Zhou, C.; Li, Z.; Yan, X.; et al. Modifying Delafossite Silver Ferrite with Polyaniline: Visible-Light-Response Z-Scheme Heterojunction with Charge Transfer Driven by Internal Electric Field. Chemical Engineering Journal 2019, 370, 1087–1100, doi:10.1016/j.cej.2019.03.282.

56. Jiang, W.; Luo, W.; Zong, R.; Yao, W.; Li, Z.; Zhu, Y. Polyaniline/Carbon Nitride Nanosheets Composite Hydrogel: A Separation-Free and High-Efficient Photocatalyst with 3D Hierarchical Structure. Small 2016, 12, 4370–4378, doi:10.1002/smll.201601546.

57. Li, W.; Tian, Y.; Zhao, C.; Zhang, Q.; Geng, W. Synthesis of Magnetically Separable Fe3O4@PANI/TiO2 Photocatalyst with Fast Charge Migration for Photodegradation of EDTA under Visible-Light Irradiation. Chemical Engineering Journal 2016, 303, 282–291, doi:10.1016/j.cej.2016.06.022.

58. Pandimurugan, R.; Thambidurai, S. Synthesis of Seaweed-ZnO-PANI Hybrid Composite for Adsorption of Methylene Blue Dye. J Environ Chem Eng 2016, 4, 1332–1347, doi:10.1016/j.jece.2016.01.030.

59. Guo, N.; Liang, Y.; Lan, S.; Liu, L.; Zhang, J.; Ji, G.; Gan, S. Microscale Hierarchical Three-Dimensional Flowerlike TiO2/PANI Composite: Synthesis, Characterization, and Its Remarkable Photocatalytic Activity on Organic Dyes under UV-Light and Sunlight Irradiation. Journal of Physical Chemistry C 2014, 118, 18343–18355, doi:10.1021/JP5044927/ASSET/IMAGES/LARGE/JP-2014-044927_0017.JPEG.

60. Faisal, M.; Ibrahim, A.A.; Bouzid, H.; Al-Sayari, S.A.; Al-Assiri, M.S.; Ismail, A.A. Hydrothermal Synthesis of Sr-Doped α-Bi2O3 Nanosheets as Highly Efficient Photocatalysts under Visible Light. J Mol Catal A Chem 2014, 387, 69–75, doi:10.1016/J.MOLCATA.2014.02.018.

61. Liu, L.; Ding, L.; Liu, Y.; An, W.; Lin, S.; Liang, Y.; Cui, W. A Stable Ag3PO4@PANI Core@shell Hybrid: Enrichment Photocatalytic Degradation with π-π Conjugation. Appl Catal B 2017, 201, 92–104, doi:10.1016/J.APCATB.2016.08.005.

62. Zhang, X.; Ai, Z.; Jia, F.; Zhang, L. Generalized One-Pot Synthesis, Characterization, and Photocatalytic Activity of Hierarchical BiOX (X = Cl, Br, I) Nanoplate Microspheres. Journal of Physical Chemistry C 2008, 112, 747–753, doi:10.1021/jp077471t.

63. Liu, J.; Wang, B.; Li, Z.; Wu, Z.; Zhu, K.; Zhuang, J.; Xi, Q.; Hou, Y.; Chen, J.; Cong, M.; et al. Photo-Fenton Reaction and H2O2 Enhanced Photocatalytic Activity of α-Fe2O3 Nanoparticles Obtained by a Simple Decomposition Route. J Alloys Compd 2019, 771, 398–405, doi:10.1016/j.jallcom.2018.08.305.

64. Zhou, L.; Zhang, W.; Chen, L.; Deng, H. Z-Scheme Mechanism of Photogenerated Carriers for Hybrid Photocatalyst Ag3PO4/g-C3N4 in Degradation of Sulfamethoxazole. J Colloid Interface Sci 2017, 487, 410–417, doi:10.1016/J.JCIS.2016.10.068.

65. Bouziani, A.; Yahya, M.; Naciri, Y.; Hsini, A.; Khan, M.A.; Sillanpää, M.; Celik, G. Development of Polyaniline Coated Titania-Hematite Composite with Enhanced Photocatalytic Activity under Sun-like Irradiation. Surfaces and Interfaces 2022, 34, 102328, doi:10.1016/J.SURFIN.2022.102328.